11th International Symposium on Turbulence and Shear Flow Phenomena (TSFP11)
Southampton, UK, July 30 to August 2, 2019

TURBULENT BOUNDARY LAYER IN A STRONG ADVERSE PRESSURE GRADIENT OVER A BODY OF REVOLUTION

N. Agastya Balantrapu[1], Christopher Hickling[2], Anthony J. Millican[3], Vidya Vishwanathan[4], Aldo Gargiulo[5]
W. Nathan Alexander[6], K. Todd Lowe[7] and William J. Devenport[8]
Kevin T. Crofton Department of Aerospace and Ocean Engineering,
Virginia Polytechnic Institute and State University, Blacksburg, Virginia 24060

Stewart Glegg[9]
Florida Atlantic University, Boca Raton, Florida 33431

ABSTRACT

A turbulent boundary layer growing over a body of revolution under a strong adverse pressure gradient is studied. Detailed measurements including the single point statistics, two-point velocity correlations, and the unsteady pressure field over the tail cone of the body are made. Evolution of the mean flow and turbulence structure under the influence of both the adverse pressure gradient and the transverse curvature are discussed; As the boundary layer decelerates, the outer regions increasingly become wake-like and the Reynolds stress profiles develop an outer peak, half-way across the boundary layer. It is shown that the large-scale motions, dominating the outer regions, are amplified by the adverse pressure gradient and these appear to control both the velocity and surface pressure convection velocities.

INTRODUCTION

Turbulent boundary layers growing over axisymmetric bodies such as the fuselage of some aircraft or marine vehicles, are very common and have been the focus of many past research efforts. Understanding the fundamental mechanisms and the interaction of these layers with the environment is important as they are a source of significant drag, noise and structural vibrations. Furthermore, these boundary layers are often ingested by rotors/propellers generating both tonal and broadband sound known as turbulence ingestion noise.

The flow over an axisymmetric body can be different from its well-studied two-dimensional counterpart in at least two ways. First, the transverse curvature cannot be ignored, especially when the boundary layer thickness is greater than the local radius of the body, and the effects can be modified in the presence of an adverse pressure gradient. Second, the flow can exhibit a complex three-dimensional behaviour even under the presence of a small angle of attack. Many past research efforts were aimed at understanding the influence of the transverse curvature in the absence of a pressure gradient, by considering the flow over an axially oriented circular cylinder (Glauert and Lighthill (1955), Willmarth and Yang (1970), Rao and Keshavan 1972, Lueptow (1990) for example). Other efforts focussed on the three-dimensional separation and evolution of an axisymmetric wake, usually by considering a 6:1 prolate spheroid with and without modifications (see Chesnakas and Simpson (1996), Gregory, Joubert et al. (2007)). However very few research efforts were directed at studying the combined effects of a transverse curvature and strong adverse pressure gradient on an attached boundary layer (Patel, Nakayama et al. 1974) and are not well understood. More recently Hammache, Browand et al. (2002) performed experiments on a body of revolution with an aft-section designed to work as a axisymmetric Stratford ramp. They focussed on the preliminary measurements of the turbulent flow and its sensitivity to the degree of adverse pressure gradient and angle of attack.

In this paper we present preliminary results from recently conducted experiments where we measured a axisymmetric boundary layer - growing over a body of revolution - under the influence of a strong adverse pressure gradient (APG). Detailed measurements of the turbulent structure including the three-component mean velocity, six-component Reynolds stresses and spectra in the adverse pressure gradient region were made. Additionally, the correlation structure was measured, including radial and circumferential correlations, and large-scale convection velocities of the unsteady streamwise velocity. The unsteady pressure field in the APG region was documented as well, including the auto-spectral densities, space-time correlations, and pressure convection velocities.

As the boundary layer decelerates under the adverse pressure gradient, the outer regions increasingly become wake-like, and the Reynolds stresses develop an outer peak towards the middle of the boundary layer. It will be shown that this is due to the increasing importance of the large-scale motions, dominating the outer regions. In the following section, the experimental arrangement and a measurement summary are presented. Next, the evolution of the mean flow, turbulence structure and correlation structure are discussed, followed by conclusions.

EXPERIMENTAL ARRANGEMENT

The measurements were performed in the anechoic test section of the Virginia Tech Stability Wind Tunnel. The aerodynamic and aeroacoustic performance of this facility is well-documented (Devenport, Burdisso et al. 2013). The Body-of-Revolution (BOR) geometry, shown in Figure 1, was inspired by prior work on a body-of-revolution with an aft ramp designed to have a Stratford-Smith pressure distribution (Hammache, Browand et al. 2002). The BOR was chosen to have a characteristic length of $D = 0.4318$ m, with a fore body comprised of a 2:1 ellipsoid nose and a constant diameter cylindrical section, with a 0.8 mm trip ring at $x/D = 0.98$. The coordinate frame used throughout this paper is shown in Figure 1, with origin at the nose. The tail section is a cone joined to the constant-diameter section with a sharp corner to ensure a thick boundary layer. Steady RANS calculations (Wang 2018) and flow visualization on a quarter-scale BOR – that set the half-apex angle at 20 degrees - were used to ensure that the boundary layer would be as thick as possible without separating. The entire assembly had a mass of 55 kg, and was mounted in the test section with a sting attached to a faired mounting post, supported by a variable-tension tether system used to adjust the angle of attack (Figure 2). Mean pressure ports in concentric rings on the nose section showed that the BOR axis was aligned with the flow to within 0.25 degrees. Additionally, a rotating total pressure

[1]agastyab@vt.edu [2]cjh88@vt.edu [3]millican@vt.edu
[4]vidya418@vt.edu [5]galdo@vt.edu [6]alexande@vt.edu
[7]kelowe@vt.edu [8]devenport@vt.edu [9]sglegg@fau.edu

rake and single hotwire surveys showed the boundary layer to be axially symmetric (outside the tether wakes) within 2% for mean velocity and 7% for turbulence intensity; For further details including the extent of the tether wakes see Hickling, Agastya Balantrapu et al. (2019). Mean pressure distribution (Figure 1) from a streamwise array of pressure taps at $Re_D = 600{,}000$ matched RANS and panel method simulations, confirming the expected mean flow behaviour, namely the sharp pressure recovery along the cone, consistent with the flow features it was designed for (Hammache, Brownand et al. 2002)

Detailed measurements of the flow over the tail cone were made at $Re_D = 600{,}000$ to obtain the evolution of the turbulent boundary layer under the strong adverse pressure gradient, discussed below.

Turbulence measurements with Hotwire Anemometry

Simultaneous measurements of the turbulence over the tail cone were made with two - single sensor hotwire probes manufactured by Auspex Corporation. The probe separation was held constant at 18.5 mm along a 9.3˚ inclination to the body axis while they were traversed over 15 streamwise stations. This ensured that the upstream probe was free from any interference, making accurate measurements of the turbulence, whereas the dual probe measurements provided large scale convection velocities. The probes were calibrated frequently in the wind tunnel to account for the temperature variation using the method of Bearman (1971).

Additionally, three-component velocities and six-component turbulence stresses and spectra were measured with a four-sensor hotwire probe manufactured by Auspex Corporation (type AVOP-4-100). Measurements were made precisely at all the points where the upstream single wire sensor was traversed, to enable cross-validation. The construction, calibration, and validation of the probes are discussed by Wittmer, Devenport et al. (1998).

The correlation structure of the boundary layer was measured towards the exit of the tail cone, with two single hotwires, in the conventional anchored probe - moving probe arrangement. Radial and circumferential correlations of unsteady streamwise velocity were measured at 4 anchor points in the boundary layer (40, 65, 75, 85% δ), at $x/D = 3.17$ obtaining the correlations as a function of separation and frequency.

All hotwire measurements were made in a horizontal plane ($x - z$) passing through the nose, away from the tether wake regions, with a Dantec Streamline 90N10 Constant Temperature Anemometer (CTA). A National Instruments device (NI DAQ 9225-9191) sampled the flow at 50 kHz obtaining 50 ensembles with 8192 samples in each. Ambient conditions including the tunnel inlet velocity, ambient pressure and temperature were acquired synchronously with hotwire measurements.

Particle Image Velocimetry (PIV)

Planar PIV measurements were made over the rear 1/3rd of the tail cone ($x/D = 2.8$ to 3.17) to obtain the spatial structure of the turbulence non-intrusively, supplementing the hotwire measurements. The flow was seeded by a LaVision Aerosol Generator which atomizes DEHS liquid to produce particles on the order of 1μm in diameter. The Stokes number for these particles in the low speed flow is much less than one, even for the smallest scales of interest. A Quantel Evergreen double-pulsed 532 nm Nd-YAG green laser pulsing at 15 Hz illuminated the seed particles, in the horizontal ($x - z$) plane passing through the body nose. A LaVision collimator along with a plano-convex lens of -50 mm focal length were used to shape the laser beam into a sheet. A LaVision Imager sCMOS camera with a Sigma EX 105mm 1:2.8D DG Macro lens, positioned outside the flow was synchronized with the laser pulses, using a LaVision Programmable Timing Unit (PTU), taking 6,000 image pairs in each measurement window.

Unsteady surface pressure sensing

The unsteady pressure field over the tail cone was measured with a streamwise linear array of 15 surface-mounted, Sennheiser microphones (type KE-4-211-2, with a 1 mm pinhole cap). The microphones were sampled simultaneously at 65 kHz with a B&K LAN XI system, obtaining the spectral densities, space-time correlations, and pressure convection velocities. The microphones have a flat frequency response from 20 – 20,000 Hz with a 140 dB dynamic range. They were installed from $x/D = 2.53$ to 3.08, spaced uniformly by 12.7 mm unless otherwise noted.

RESULTS AND DISCUSSION

Results will be discussed in the co-ordinate system (x, y, z), shown in Figure 1. With origin at the nose, the x – axis is aligned with the BOR axis, the y-axis is oriented vertically upward, and the z – axis completing a right-handed co-ordinate system. The mean velocities along x, y, z axes will be identified by U, V, W respectively. Similarly, the unsteady velocities are referred in the lower case - u, v, w. The streamwise mean and unsteady velocity are U_s and u_s respectively. The tunnel reference velocity at the inlet is U_∞.

In the corresponding cylindrical co-ordinate system (x, r, θ), r is the radial distance from the x-axis and θ is the polar angle, measured from the vertical (y-axis) by the right-hand rule.

Mean flow over body

Before entering the strong adverse pressure gradient (APG) zone at the rear, the flow experiences a favourable pressure gradient (FPG) over the nose followed by a near zero pressure gradient (ZPG) over the midbody – shown by the mean pressure distribution in Figure 1. Additionally, a strong acceleration at the sharp corner might affect the flow history. Before entering the tail-cone, the boundary layer over the cylindrical mid-body is $7.9\,mm$ thick (δ/D=0.009), with peak measured turbulence intensity of $0.08U_\infty$. The displacement thickness δ_1 estimated using the planar definition is 0.10δ and the momentum thickness $\delta_2 = 0.07\delta$, yielding a shape factor $H = 1.44$.

Downstream the corner, the flow decelerates rapidly over the 20° tail cone due the adverse pressure gradient, seen in the streamwise mean velocity contours in Figure 3. At the exit ($x/D = 3.17$) the boundary layer is 79.5 mm thick, growing about ten times over a distance of $1.2D$. Furthermore, the edge velocity just outside the boundary layer decreases correspondingly, by $0.3\,U_\infty$ over the tail cone: from $1.2\,U_\infty$ to $0.9U_\infty$. Figure 4 shows the in-plane flow orientation (U, W) over the tail cone, estimated from the quad-wire probe. Closer to the wall, the flow is aligned with the BOR surface, suggesting that the boundary layer is attached. However, the flow diverges as we move away from the wall and is more aligned with the BOR axis instead, consistent with the strong adverse pressure gradient.

The strength of an APG has been characterized by different non-dimensionalized parameters in the past. Skin friction-based parameters (such as, Clauser (1954), Huffman and Bradshaw (1972)), are not expected to be as relevant when the APG is

strong (Durbin and Belcher 1992). Instead, for two-dimensional flows, Castillo and George (2001) proposed a 'pressure gradient parameter' $\Lambda = -\delta/(U_e\, d\delta/dx) * dU_e/dx$, based on the freestream pressure gradient. Figure 5 shows the Λ distribution over the tail cone. The adverse pressure gradient is initially strong with $\Lambda \approx 0.3$ and appears to weaken gradually as the flow expands downstream. Towards the end of the tail cone, Λ drops slightly below zero – an effect of the local favorable pressure gradient imposed by the downstream support shaft. Furthermore, transverse curvature effects might be important in addition to APG, particularly towards the rear where the boundary layer thickness is greater than the local radius; At $x/D = 3.17$, the boundary layer thickness is 2.5 times the local radius of curvature ($\delta/r_s = 2.5$) (Figure 3). Note that the mean velocity from the single hotwire, quadwire and PIV are in agreement in the boundary layer suggestiong no significant influence of probe interference.

Figure 6 shows the streamwise mean velocity profiles (from single hotwire) over the tail cone region, corresponding to the contours of Figure 3. The vertical axis represents the normalized distance from the surface ($|z - z_s|$), perpendicular to the BOR axis; the horizontal axis represents the velocity normalized by the local edge velocity(U_s/U_e). The character of these profiles changes substantially, with the velocity deficit strengthening as the flow travels downstream under the APG. The velocity deficit profiles over the rear third of the tail cone from PIV measurements are shown in Figure 7(a); with deficit on the vertical axis and normalized distance on the horizontal axis. Clearly, U_e and δ do not collapse the deficit profiles in this region. While a detailed examination is necessary to determine any self-similarity in the mean flow, our initial observations show that the outer region velocity scale $U_{ZS} = U_e\delta_1/\delta$, developed by Zagarola and Smits (1998) is promising (see Figure 7(b)). This has been previously observed in two-dimensional APG flows, shown by several researchers including, Castillo and George (2001), Maciel, Rossignol et al. (2006). However, Maciel observed these defect profiles to collapse but to a unique curve for different flow conditions.

Turbulence Structure

Figure 8 shows the streamwise Reynolds normal stress profiles over the tail cone, corresponding to the mean velocity profiles in Figure 6. The horizontal axis represents the stresses normalized on the local edge velocity where as the vertical axis represents the distance from the surface, perpendicular to the BOR axis (or x-axis). Similar to the mean velocity profiles, the character of the Reynolds stresses evolves significantly with an outer peak appearing downstream. This peak weakens and shifts higher up, from around 0.4δ at the begnning to about 0.55δ at the tail cone exit. Such an outer peak is a typical feature of APG flows, as observed by many researchers, such as Nagano, Tagawa et al. (1993), and the location of this peak is usually between $0.4\delta - 0.6\delta$, perhaps depending on the strength of APG. Regarding self-similarity, the U_{ZS} scale does not collapse the Reynolds stress profiles any better than U_e.

Spectral analysis studies in APG flows (Bradshaw (1967); Harun, Monty et al. (2013)) suggest that the large scale motions intensify across the boundary layer as adverse pressure gradient increases. These intense large-scale motions, dominant in the outer regions, are believed to control the turbulent activity and are responsible for the outer secondary peak in the Reynolds stresses, as we observed earlier. Figure 9 shows the spectral breakdown of the streamwise Reynolds stresses, at three axial locations: Just upstream of the corner ($x/D = 1.97$), half-way through the tail cone ($x/D = 2.69$) and the exit ($x/D = 3.17$) (Figures 9(a), (b), (c) respectively). The frequency is shown on the horizontal axis, and height from the surface is shown on the vertical axis. The contour levels reveal the spectral density in dB per Hz. The turbulent structure is modified as the flow progresses over the tail cone. Before entering the APG region – in Figure 9(a) – the energy is highest at the lower frequencies (large scale motions), closest to the wall ($|z - z_S|/\delta \approx 0$). Moving away from the wall the energy decreases monotonically, across the entire frequency range; This structure is somewhat similar to a zero-pressure gradient turbulent boundary layer. At the tail cone exit (Figure 9(c)) the lower frequencies do contain the peak energy but this energy is concentrated further away, and distinctly above, the wall – corresponding to the outer peak observed in the Reynolds stress profile ($|z - z_S|/\delta \approx 0.55$) – similar to the observations of Harun, Monty et al. (2013).

Furthermore, these overriding large scale motions appear influence the small-scale motions closer to the wall, described in the following section.

Correlation Structure

Figure 10 shows the contours of the phase convection velocities of the unsteady streamwise velocity, obtained from the two-probe measurements, explained in the Experimental Arrangement section. The contour levels represent the convection velocity normalized on the local mean velocity (U_s) in the boundary layer. It appears that the coherent structures in the outer portion of the boundary layer travel at the local mean speed whereas those in the inner region appear to travel faster than the local mean speed. Closer to the wall ($|z - z_S|/\delta \approx 0.1$), the convection velocity is over $1.5U_s$. Furthermore, these near wall convection velocities match with the surface pressure phase convection velocities. Recently, Drozdz and Elsner (2017) observed increased convection velocities closer to the wall, under an adverse pressure gradient, about $2U_s$ in the buffer region. They attributed it to the influence from the overriding large scale motions, suggesting the small-scale turbulence production could be driven by the higher speed, large scale turbulence in a boundary layer under a strong APG.

The detailed distribution and geometry of the large-scale motions in a turbulent boundary layer can be experimentally estimated from two-point velocity correlations; but is complicated since the boundary layer (in our case) is radially inhomogeneous and anisotropic, in addition to rapidly evolving in the streamwise direction. Nonetheless, subsets of such a measurement provide useful insight into the structure of turbulence. We measured the radial and circumferential correlations of the streamwise unsteady velocity at the tail cone exit (x/D=3.17), using the anchored probe – moving probe arrangement. Figure 11 (a) shows the radial correlation measurements for four anchor positions ($40,\ 65,\ 75,\ 85\%\ \delta$), with the moving probe traversed outward at each anchor point, obtaining the correlations as a function of separation and frequency. The zero-time delay radial correlations are shown in Figure 11(b); The cross-correlation coefficient ($\rho_{u_s u'_s}$) between the two probes is represented on the vertical axis, and the corresponding radial separation ($r - r'$) normalized on δ is shown on the horizontal axis. The radial correlations decay monotonically with increasing separation, reaching 10% level at about a separation of 0.2δ for all anchor positions. However, at the outer positions ($75, 85\%\ \delta$), the correlations develop slightly negative lobes at larger separations. The radial length scales of the streamwise velocity (estimated by integrating the correlation curves) appear to increase on moving towards the wall. At $85\%\ \delta$ the length scale is about 0.06δ, increasing to 0.09δ towards the middle of the boundary layer.

Figure 11(d) shows the correlations as a function circumferential separation, in a format similar to the radial correlations; the horizontal axis represents the circumferential separation ($s = r\Delta\theta$) normalized on the boundary layer thickness. The cross-correlation coefficients decay monotonically at each anchor position – faster than the radial correlation coefficients – reaching 10% levels at about 0.1δ, depending slightly on the anchor position. Furthermore, the negative tails (-5%) at larger separations ($0.15\delta - 0.4\delta$) are stronger than the radial case. This suggests the circumferential length scales are substantially smaller and are indeed about half the corresponding radial length scales.

CONCLUSIONS

A turbulent boundary layer growing over a body of revolution under a strong adverse pressure gradient is measured experimentally. Evolution of the mean flow, single point turbulence statistics and the correlation structure is discussed. As the axisymmetric boundary layer decelerates rapidly over the rear tail cone, the outer regions of the boundary layer increasingly become wake-like, with the mean velocity defect strengthening downstream. The Reynolds stresses develop a characteristic outer peak towards the middle of the boundary layer. Velocity spectra show that this is due to the increasing importance of the large scale motions dominating the outer regions and indeed these appear to dominate both the velocity and surface pressure convection velocities.

ACKNOWLEDGEMENTS

We acknowledge the support from the Office of Naval Research, particularly Drs. Ki-Han Kim and John Muench, in supporting this work under grants N00014-17-1-2698 and N00014-17-1-2682. We thank the Aerospace and Ocean Engineering Machine Shop staff headed by Mr. James Lambert, in leading the fabrication and instrumentation hardware efforts. We also thank Dr. Aurilien Borgoltz, Bill Oetjens, Mathew Ruda, Nandita Hari, James MacDonald among others for assistance during the wind tunnel experiments. We are grateful to Drs. Meng Wang, William Blake and Jason Anderson, and Mr. Michael Marcolini, for their helpful advice and support on this project.

REFERENCES

Bearman, P. W. (1971). "Corrections for the effect of ambient temperature drift on hot-wire measurements in incompressible flow." DISA Information **11**: 25-30.

Bradshaw, P. (1967). "Turbulence structure of equilibrium boundary layers." Journal of Fluid Mechanics **29**(Part 4): 625-645.

Castillo, L. and W. K. George (2001). "Similarity Analysis for Turbulent Boundary Layer with Pressure Gradient: Outer Flow." AIAA Journal **39**(1): 41-47.

Chesnakas, C. J. and R. L. Simpson (1996). "Measurements of the Turbulence Structure in the Vicinity of a 3-D Separation." Journal of Fluids Engineering **118**(2): 268-275.

Clauser, F. H. (1954). "Turbulent boundary layer in adverse pressure gradient." J. Aero. Sci. **21**: 91-108.

Devenport, W. J., R. A. Burdisso, A. Borgoltz, P. A. Ravetta, M. F. Barone, K. A. Brown and M. A. Morton (2013). "The Kevlar-walled anechoic wind tunnel." Journal of Sound and Vibration **332**(17): 3971-3991.

Drozdz, A. and W. Elsner (2017). Convection velocity variation as a result of amplitude modulation phenomena. Progress in Turbulence VII: iTi Conference in Turbulence 2016, 7-9 Sept. 2016, Cham, Switzerland, Springer International Publishing.

Durbin, P. A. and S. E. Belcher (1992). "Scaling of adverse-pressure-gradient turbulent boundary layers." Journal of Fluid Mechanics **238**: 699-722.

Glauert, M. and M. J. Lighthill (1955). "The axisymmetric boundary layer on a long thin cylinder." Proc. R. Soc. Lond. A **230**(1181): 188-203.

Gregory, P., P. Joubert and M. Chong (2007). "Measurements of turbulent crossflow separation created by a curved body of revolution." Journal of Fluid Mechanics **589**: 353-374.

Hammache, M., F. Browand and R. Blackwelder (2002). "Whole-field velocity measurements around an axisymmetric body with a Stratford–Smith pressure recovery." Journal of Fluid Mechanics **461**: 1-24.

Hammache, M., F. K. Browand and R. F. Blackwelder (2002). "Whole-field velocity measurements around an axisymmetric body with a Stratford-Smith pressure recovery." Journal of Fluid Mechanics **461**: 1-24.

Harun, Z., J. P. Monty, R. Mathis and I. Marusic (2013). "Pressure gradient effects on the large-scale structure of turbulent boundary layers." Journal of Fluid Mechanics **715**: 477-498.

Hickling, C., N. Agastya Balantrapu, A. Millican, J., W. Nathan Alexander, W. J. Devenport and S. A. L. Glegg (2019). Turbulence Ingestion into a Rotor at the Rear of an Axisymmetric Body. 25th AIAA/CEAS Aeroacoustics Conference, 2019, May 20, 2019 -May 16 2019, Delft, The Netherlands, American Institute of Aeronautics and Astronautics Inc, AIAA.

Huffman, G. D. and P. Bradshaw (1972). "A note on von Kármán's constant in low Reynolds number turbulent flows." Journal of Fluid Mechanics **53**(1): 45-60.

Lueptow, R. M. (1990). "Turbulent boundary layer on a cylinder in axial flow." AIAA journal **28**(10): 1705-1706.

Maciel, Y., K.-S. Rossignol and J. Lemay (2006). "Self-similarity in the outer region of adverse-pressure-gradient turbulent boundary layers." AIAA Journal **44**(11): 2450-2464.

Nagano, Y., M. Tagawa and T. Tsuji (1993). Effects of adverse pressure gradients on mean flows and turbulence statistics in a boundary layer. Proceedings of the 8th International Symposium on Turbulent Shear Flows, Sep 9 - 11 1991, Munich, Germany, Publ by Springer-Verlag New York.

Patel, V., A. Nakayama and R. Damian (1974). "Measurements in the thick axisymmetric turbulent boundary layer near the tail of a body of revolution." Journal of Fluid Mechanics **63**(2): 345-367.

Rao, G. and N. Keshavan (1972). "Axisymmetric turbulent boundary layers in zero pressure-gradient flows." Journal of Applied Mechanics **39**(1): 25-32.

Wang, M. (2018). Personal Communication.

Willmarth, W. W. and C. S. Yang (1970). "Wall-pressure fluctuations beneath turbulent boundary layers on a flat plate and a cylinder." Journal of Fluid Mechanics **41**(1): 47-80.

Wittmer, K. S., W. J. Devenport and J. S. Zsoldos (1998). "A four-sensor hot-wire probe system for three-component velocity measurement." Experiments in Fluids **24**(5): 416-423.

Zagarola, M. V. and A. J. Smits (1998). "Mean-flow scaling of turbulent pipe flow." Journal of Fluid Mechanics **373**: 33-79.

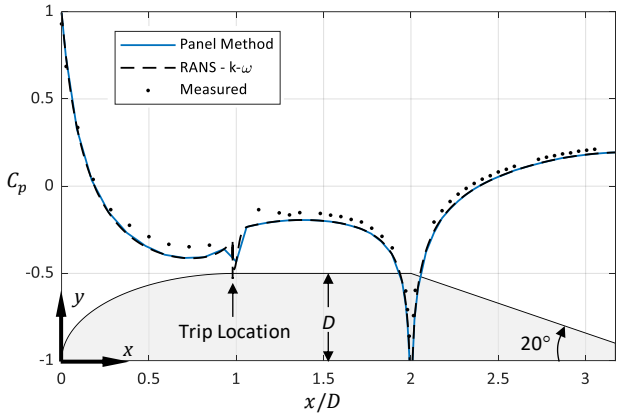

Figure 1:Virginia Tech Body of Revoution (BOR) geometry and mean pressure distribution for Re_D = 600,000. Flow is left to right along x-axis. Co-ordinate frame origin is at the nose

Figure 2: BOR installed in the Stability Wind Tunnel Kevlar-walled anechoic test section, including supporting tethers, sting, and mounting post.

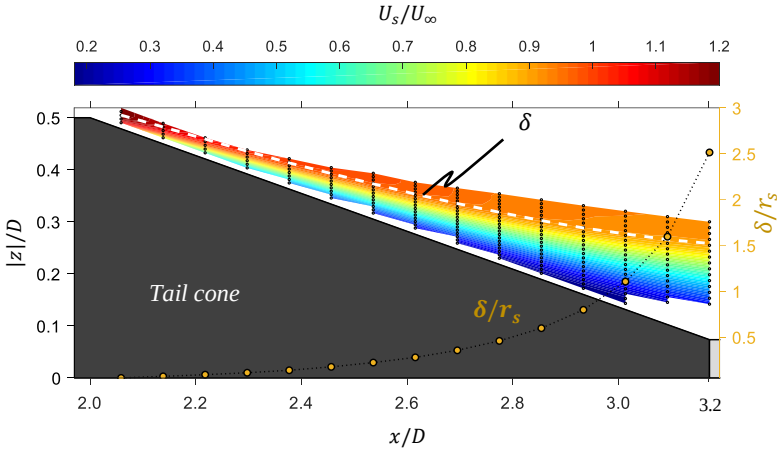

Figure 3: Contours of streamwise mean velocity over the tail cone region of the BOR showing the evolution of the mean flow and boundary layer thickness. Shown also is the boundary layer growth with respect to the local radius of the body (right vertical axis)

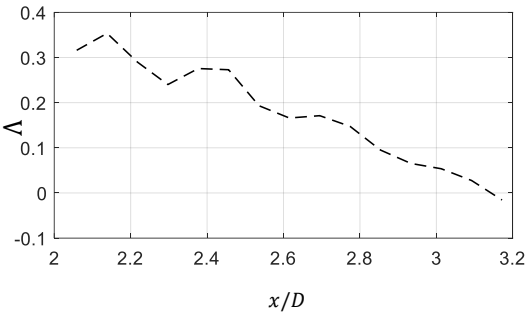

Figure 5: Distribution of the pressure gradient parameter Λ over the tail cone region of the BOR.

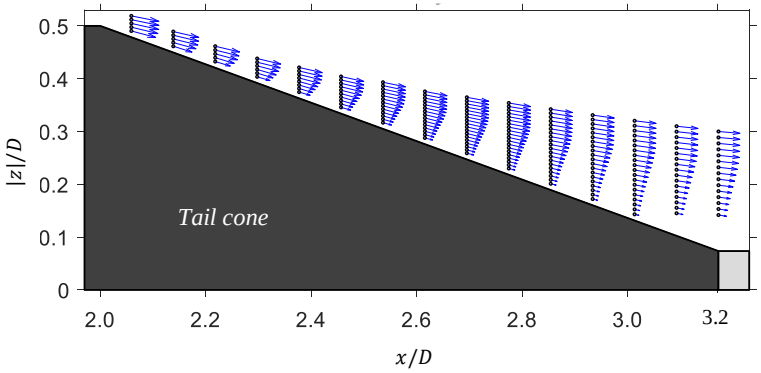

Figure 4: In-plane mean velocity vectors from quadwire measurements, showing the flow orientation with respect to the tail cone

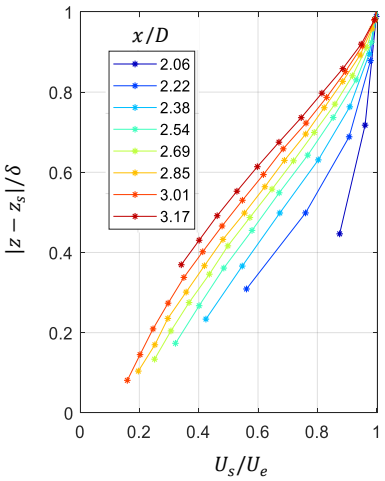

Figure 6: Streamwise mean velocity profiles over the tail cone. Velocity on the horizontal axis, normalized on the local edge velocity. Distance from surface, normalized on the local boundary layer thickness, shown in vertical axis

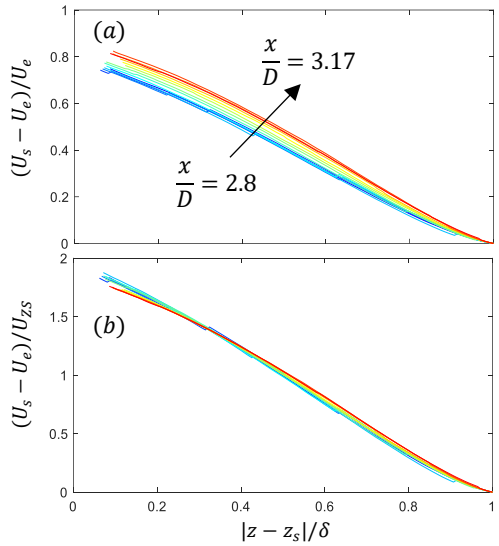

Figure 7: Streamwise mean velocity defect profiles versus height from the BOR surface. Colors change from blue to red as we go downstream over the rear third of the ramp. In (a) the defect is normalized on the local edge velocity. In (b) the defect is normalized on $U_{ZS} = U_e\delta_1/\delta$

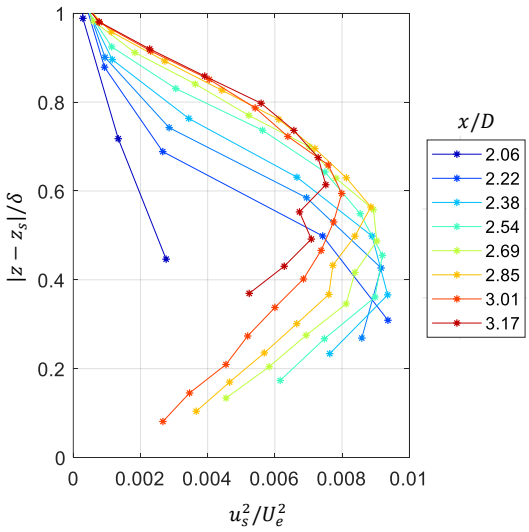

Figure 8: Streamwise Reynolds normal stress profiles, normalized on the local edge velocity

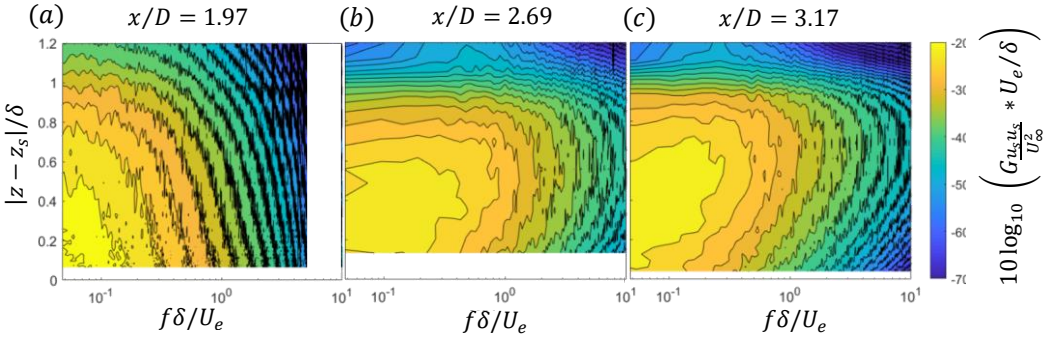

Figure 9: Contours of the streamwise unsteady velocity spectra, for representative locations on the tail cone – (a) x/D =1.97, (b) 2.69, (c) 3.17,; In each figure, vertical axis represents the height from the surface normalized on δ. Horizontal axis represents the normalized frequency $f\delta/U_e$

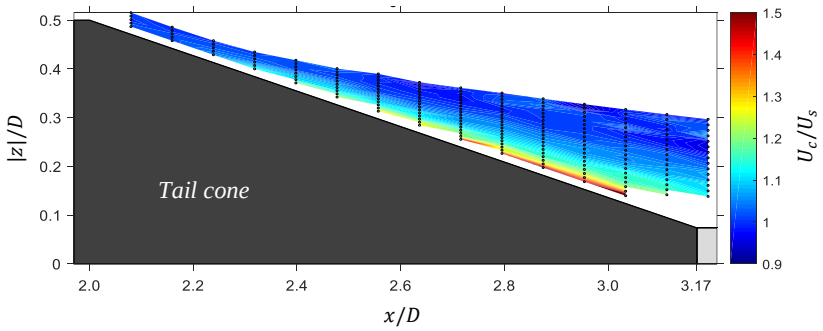

Figure 10: Contours of convection velocity (U_c) over the tail cone of the BOR. The velocity is normalized by the local mean (between the two probes) velocity

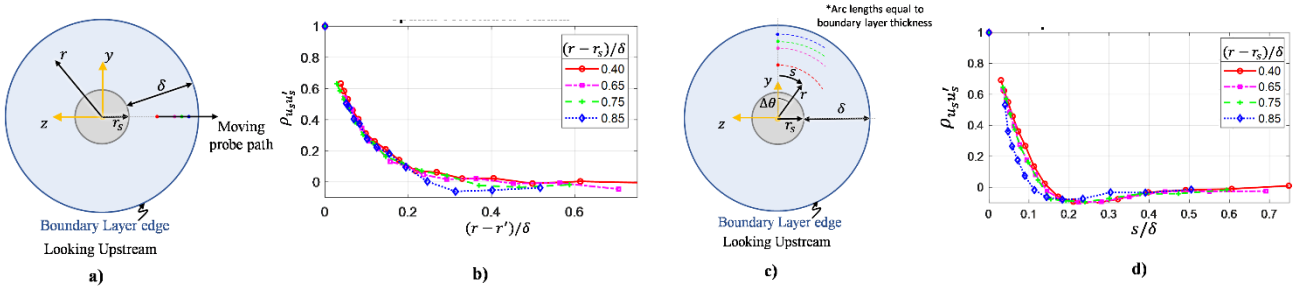

Figure 11: Zero-time delay, cross-correlation coefficients of the unsteady streamwise velocity, from hotwire measurements at the tail cone exit plane ($x/D = 3.17$). (a) shows the measurement plane, anchor probe positions, and the moving probe path for the radial correlation measurements. (b) shows the cross-correlation coefficient for all anchor probe positions, as a function of separation distance normalized on the boundary layer thickness. Similarly, (c) shows the measurement plane for circumferential correlation measurements. (d) shows the circumferential correlation coefficient as a function of circumferential separation